71st Annual Congress
ISSN 1516-392X
abm week 2016

MICRO-ABRASIVE WEAR BEHAVIOUR OF LOW-TEMPERATURE PLASMA CARBURIZED AISI 420 MARTENSITIC STAINLESS STEEL*

Cristiano José Scheuer[1]
Rodrigo Perito Cardoso[2]
Júlio César Klein das Neves[3]
Sílvio Francisco Brunatto[4]

Abstract

Experiments were carried out aiming to study the influence of micro-abrasive wear test variables and plasma treatment parameters, on the tribological characteristics of low-temperature plasma carburized AISI 420 steel. The first part of this study was conducted in order to evaluate the influence of abrasive particle size, normal load and counter body rotation speed on carburized sample wear behavior; and the second part was conducted in order to evaluate the treatment temperature and time effect on carburized samples wear behavior. Plasma carburizing treatments were performed at 8 and 12 h, for temperatures ranging from 350 to 500°C; and at constant temperatures of 400°C for times between 12 to 48h, and for 450°C for times of 4 to 16h. Micro-abrasive wear test were performed by mean of a calowear ball-cratering equipment using a polished ball of AISI 52100 steel rotating at 80, 120 and 160 rpm, for sliding distances from 2.6 to 104.2 m. Alumina abrasive particles with sizes of 0.05, 0.3 and 1.0 μm were employed. The normal loads applied on this study were 0.1, 0.3 and 0.5 N. Carburized sample was characterized by mean of OM, XRD and hardness measurements. Worn crater characteristics were evaluated by confocal laser microscopy. Results showed that the transient wear regime prevails along the outer layer length (composed by Fe_3C and α'_C), and the steady-state wear stabilizes in the diffusion layer region (composed by α'_C). It was verified that the wear rate and wear coefficient decreases with treatment temperature in the range of 350–450°C and increase for 500°C. It was also verified that the wear rate and wear coefficient decreases with treatment time in the range of 12–36 h (for 400°C cycle) and 4–12 h (for 450°C cycle), and increase for larger treatment times due the chromium carbide precipitation. It was also found that the wear coefficient increases with the increase of abrasive particle size, and decrease with the increase in counter body rotation speed and normal load. Lastly, the analysis of the worn craters indicates the occurrence of grooving and micro-rolling abrasion wear mechanisms.

Keywords: Ball-cratering test; Grooving abrasion; Micro-rolling abrasion; Low-temperature plasma carburizing; Martensitic stainless steel.

[1] *Mechanical Engineer, D.Sc., Assistant Professor, Industrial Technical College, Universidade Federal de Santa Maria, Santa Maria, RS, Brazil.*
[2] *Mechanical Engineer, D.Sc., Assistant Professor, Mechanical Engineer Department, Universidade Federal do Paraná, Curitiba, PR, Brazil.*
[3] *Metallurgical Engineer, D.Sc., Professor, Academic Department of Mechanics, Universidade Tecnológica Federal do Paraná, Curitiba, PR, Brazil.*
[4] *Mechanical Engineer, D.Sc., Associate Professor, Mechanical Engineer Department, Universidade Federal do Paraná, Curitiba, PR, Brazil.*

** Technical contribution to the 71º Congresso Anual da ABM – Internacional and to the 16º ENEMET - Encontro Nacional de Estudantes de Engenharia Metalúrgica, de Materiais e de Minas, part of the ABM Week, September 26th-30th, 2016, Rio de Janeiro, RJ, Brazil.*

1 INTRODUCTION

Plasma assisted treatments are commonly applied to improve surface properties of steels, such as wear and corrosion resistance [1]. Through this technique a large concentrations of interstitial alloying elements may be introduced into the material surface [2]. The application of plasma-assisted treatments as carburizing and nitriding on stainless steel, promotes an increase in wear and corrosion resistance of these alloys, when treatments are conducted under low-temperature condition and for short times. However, when treatment is carried out at high temperature or for excessive time, the wear resistance increase is accompanied by the reduction of the treated surface corrosion resistance [3]. The corrosion resistance decrease occurs due to precipitation of chromium carbide/nitride, resulting in the sensitization of the treated surface [4]. The increased corrosion and wear resistance observed for low-temperature plasma treatments of stainless steels is attributed to metastable phases formation on the treated surface [5]. In the case of low temperature plasma nitriding application on martensitic stainless steels, the nitrogen incorporation leads to the formation of nitrogen expanded martensite phase (α'_N), which presents high wear [6,7], corrosion [7-9], and fatigue resistance [10]. For low-temperature plasma carburizing of martensitic stainless steel, the carbon introduction on the steel surface promotes the formation of carbon expanded martensite phase (α'_C) [11-13], whose tribological properties and corrosion resistance remain undetermined.

Wherefore, on present project the micro-abrasive wear resistance of carbon expanded martensite generated on AISI 420 martensitic stainless steel by low-temperature plasma carburizing was studied. Considering the micro-abrasive test variables influence on wear process, already reported by other authors, as contact load [14-18], sliding distance [14,16,19-21], sphere rotation speed [15,16,18,22], and abrasive characteristics [17,19,23,24], the first part of this project aims study the effect of abrasive particle size, counter body rotation speed and normal load on the wear behaviour (rate, coefficient and mechanism) of carburized AISI 420 steel. Similarly, considering the effect of plasma carburizing temperature and time on the microstructural features and mechanical properties of AISI 420 steel (reported by [13]), the second part of this project aims to study the effects of these parameters on micro-abrasive wear behaviour of treated samples.

2 MATERIAL AND METHODS

Cylindrical samples of 10 mm in height and 50.8 mm in diameter were cut from an AISI 420 steel commercial rod (composition obtained by X-ray fluorescence, in wt.%: 0.17% C, 0.70% Mn, 0.50% Si, 12.2% Cr, 0.23% P, 0.03% S, and Fe balance). Samples were air quenched from 1050 °C, after 0.5 h at the austenitizing temperature. After heat treatment, samples were ground using SiC sandpaper ranging from 100 to 1200 grade and polished using 1 µm Al_2O_3 abrasive suspension. Finally, samples were alcohol cleaned in ultrasonic bath and then introduced into the discharge chamber.

A schematic representation and the detailed description of the plasma apparatus used in the present work is described and shown in reference [13]. On this system, samples were placed on the cathode and negatively biased at 700 V. Aiming to remove the native oxide layer from samples surface, before carburizing, specimens were plasma sputter-cleaned in a gas mixture of 80% H_2 + 20% Ar, under a pressure

of 400 Pa, at 300°C for 0.5 h. Plasma carburizing was carried out using a gas mixture composed of 99.5% (80% H_2 + 20% Ar) + 0.5% CH_4, in volume. The total gas flow rate and pressure were fixed at 1.66×10^{-6} Nm^3s^{-1} (100 sccm) and 400 Pa, respectively. Samples were carburized at temperatures of 350, 400, 450 and 500 °C, for treatment time of 8 and 12 h; and at fixed times of 400° C for 12, 24, 36 and 48 h, and 450° C for 4, 8, 12 and 16 h.

Micro-abrasive wear test were performed using a CSM CaloWear® micro-abrasion ball-cratering equipment. Alumina abrasive suspension (Al_2O_3) with concentration of 0.11 g/cm^3 and particle size of 0.05, 0.3 and 1.0 μm were used to perform the study of abrasive particle size effect. In order to prevent the decantation of abrasive slurry, the suspension was continuously agitated during the wear test by means of stirring apparatus attached to the micro-abrasion equipment, and pumped to the ball/sample interface by a peristaltic pump, at a flow rate of 0.2°drop/s. A polished ball of AISI 52100 steel with 25.4 mm diameter was used as counter body, being rotated at a speed of 80, 120 and 160 rpm (sphere rotation speed study), generating a velocity between the sphere and the sample surface of approximately 0.1, 0.16 and 0.21 ms^{-1}. The diameters of the worn craters were measured after sliding distances of 2.6, 5.2, 7.8, 10.4, 15.6, 31.0, 46.8, 62.4, 78.5 and 104.2 m. For measuring the dimensions of wear crater and analyzing the worn region (aiming to identify the abrasion wear modes), a confocal laser scanning microscope (Olympus LEXT OLS 3000), was used. From measuring of the worn craters diameter, the wear volume was determined for each test condition applying the equations suggested by Rutherford and Hutchings [22]. The average wear coefficient was determined from the line slope generated by the data linearization of the function $V = f(L, N)$, where, V is the wear volume; L is the sliding distance; and N the normal force. Normal load of 0.1, 0.3 and 0.5 N was employed in this work (contact load study). The worn region (wear crater) was analyzed by confocal laser scanning microscope (Olympus LEXT OLS 3000), aiming to identify the abrasion wear mode.

For microstructural analysis, sample was prepared by conventional metallographic procedure. After polishing, the cross-sectioned specimen was etched using Marble's reagent (4g $CuSO_4$ + 20 ml HCl + 20 ml H_2O). The microstructure was examined using an Optical Microscope (Olympus BX51M), and the thickness of the observed outer layer was determined by taking the mean of ten measurements using micrographs images. The identification of the phases present in the treated layers was carried out by X-ray diffractometry (XRD), using a Shimadzu XRD 7000 X-ray diffractometer with a Cu Kα X-ray tube (λ = 0.17889 nm) in the Bragg–Brentano configuration. The diffraction lines were taken with 2θ in the range of 30-60° with steps of 0.1°/min. Profile hardness and surface hardness measurements were taken by using a Shimadzu Micro Hardness Tester HMV2T, applying loads of 10 gf and 25 gf, respectively, and a peak-load contact of 15 s. The hardness values are a mean of five measurements.

3 RESULTS AND DISCUSSION

3.1 Microstructural and mechanical characterization

Cross section micrograph of samples plasma carburized for 12 h at (a) 450 and (b) 500°C are shown in Figure 1. It can be observed that for the lower temperatures the outer layer presents higher resistance to the chemical etchant if compared to the

bulk. However, for the higher temperatures (around 500°C) the outer layer presents lower resistance if compared to the bulk. It is an evidence of chromium carbide precipitation causing sensitization, what is well confirmed for the samples treated at 500°C (Figure 1b). Similar behavior was observed for samples treated at 8 h.

Arrhenius plots of outer layer thickness for samples treated at 8 and 12 h are shown in Figure 2 (a). It is noted that the thickness increases with increasing treatment temperature, which is characteristic of diffusion controlled process. The activation energy for the carbon diffusion in AISI 420 steel under the treatment conditions employed here is approximately 85 kJ/mol. Additionally, at high temperatures the limiting process for layer growth seem to tend to have the same activation energy, what is coherent since the process tends to the equilibrium.

The outer layers thickness variation as a function of the square root of treatment time are shown in Figure 2 (b). It is noted that the thickness increases with increasing treatment time, which is characteristic of diffusion controlled process. The apparent diffusion coefficient of carbon in the martensite lattice shows values of 0.396 μm/h and 0,543 μm/h, for the treatment performed at 400 and 450 °C, respectively.

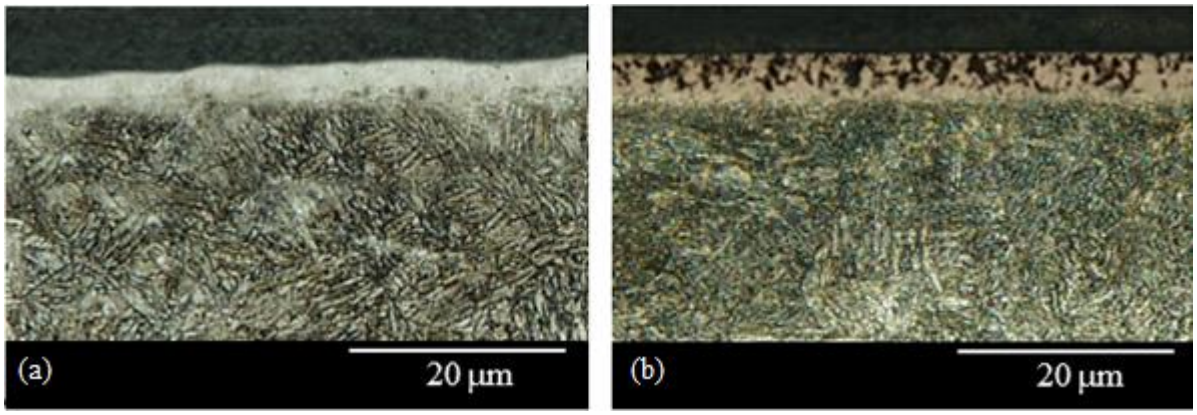

Figure 1. Cross-section micrographs of AISI 420 steel plasma carburized for 12 h at (a) 450 and (b) 500°C.

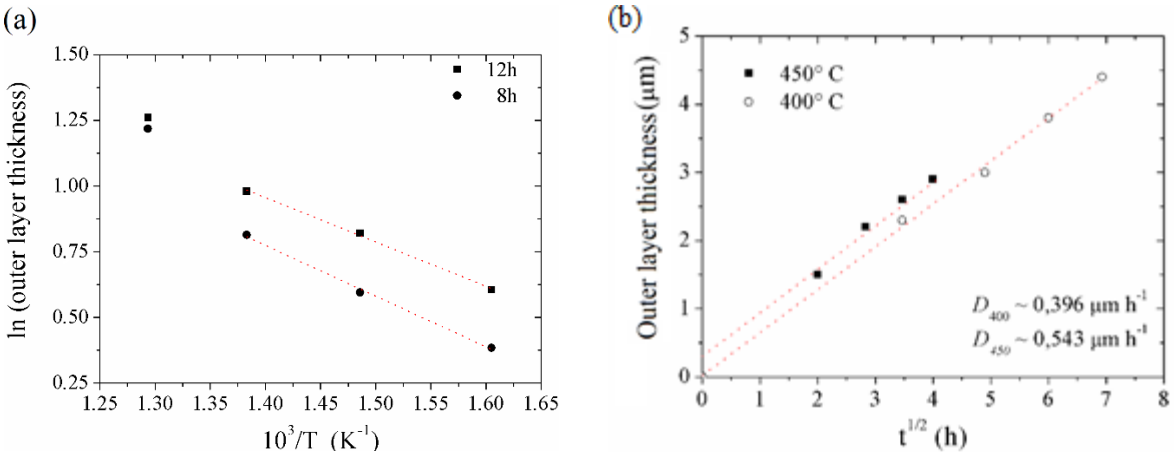

Figure 2. (a) Arrhenius plot; and (b) outer layer thickness *vs* $t^{1/2}$ for AISI 420 steel plasma carburized.

Surface hardness as a function of the treatment temperature for samples carburizing at 8 and 12 h are present in Figure 23 (a). It appears that the hardness increases linearly with the treatment temperature for the two studied cycles. These hardness

increases is due to the increased carbon content in solid solution, and due to the formation of Fe_3C, Cr_7C_3 and $Cr_{23}C_6$ phases (as shown by the XRD data present in Figure 4 (a).

Surface hardness as a function of the treatment time for samples carburizing at 400 and 450°C are present in Figure 23 (b). It appears that the hardness increases linearly with the treatment time in intervals between 12 to 36 h for treatments performed at 400 °C, and 4 to 12 h for treatments carried out at 450 °C. These hardness increases is due to the increased carbon content in solid solution, and due to the formation of Fe_3C phase (as shown by the XRD data present in Figure 4 (b). The hardness decrease, on the other hand, occurs due to the precipitation of chromium carbides, which reduces the carbon content in solid solution, leading to a compressive residual stresses reduction, and consequently, the materials hardness.

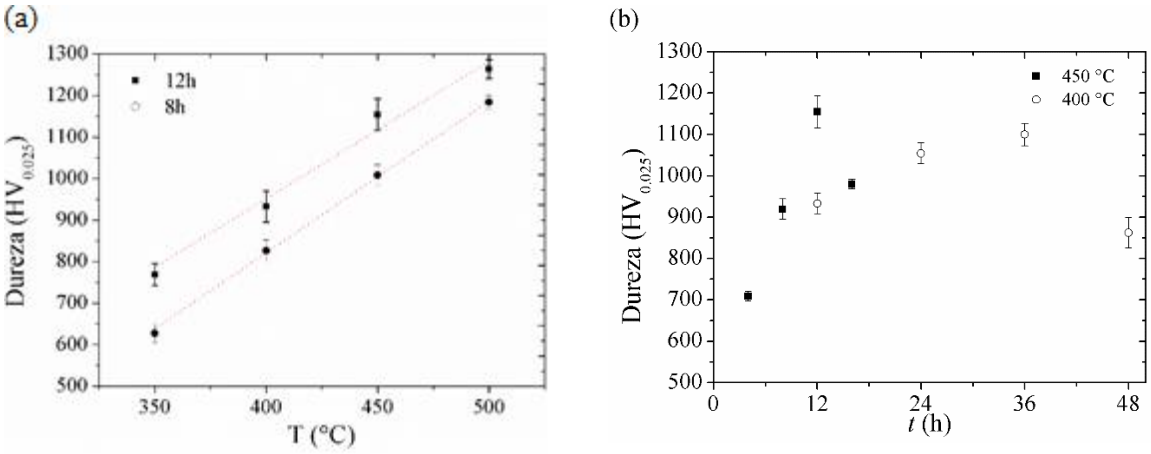

Figure 3. Surface hardness of the outer layer produced on AISI 420 steel as a function of the carburized temperature (a) and times (b).

Figure 4 (a) present the X-ray diffraction patterns of untreated (as-quenched) and samples plasma carburized for 12 h at 350 to 500 /C. The as-quenched sample presents one peak (at 2θ angle of 44.9°) attributed to the martensite phase (α'). After carburizing treatment these α' peak phase was broadened and slightly shifted to lower 2θ angles (see Figure 4 (a,b) detail), indicating that the martensite lattice parameter was expanded by carbon diffusion (α'c). In addition, the remaining peaks occurring at 37.2°, 39.3°, 40.3°, 42.5°, 43.3°, 45.6°, 48.8°, 51.5°, 55.7° and 57.7°correspond to the Fe_3C phase. The occurrence of Cr_7C_3 and $Cr_{23}C_6$ phase could be suggested in the present case by the diffraction peaks occurring for 2θ angles of 37.2°, 39.3°, 43.3°, 48.8° and 51.5°, but it should be noted that such peaks could be also indexed for the Fe_3C phase. For 500 °C conditions the most of the carbon present in the body-centered tetragonal (b.c.t.) martensite cell precipitates as chromium carbide during carburizing treatment, promoting the transformation from b.c.t to b.c.c. (*body-centered cubic*) cell. Figure 4 (b) present the X-ray diffraction patterns of untreated (as-quenched) and samples plasma carburized at 400°C for 12 to 48 h. For samples treated in times less than 36 h, there is the presence of the same phases identified for samples treated at temperatures under 450°C. As for the sample treated at 500°C, the sample carburized for 48 h the martensite phase decomposition was observed. The X-ray diffraction patterns for the other studied conditions can be viewed in [13].

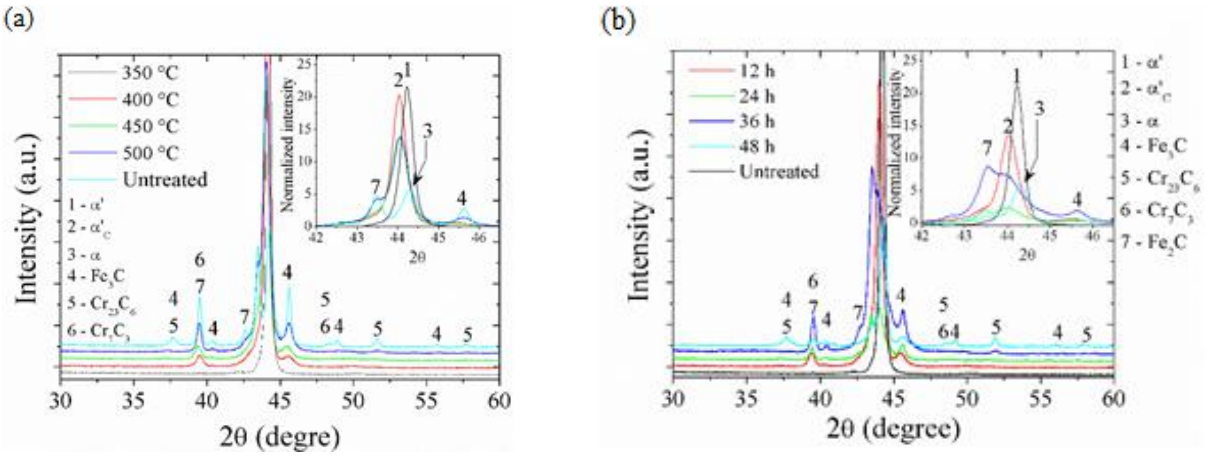

Figure 4. X-ray diffraction patterns of AISI 420 steel samples plasma carburizing at 350 to 500°C for 12 h (a); and for 12 to 24 h at 400°C (b).

Figure 5 (a) shows the hardness profiles of the samples carburized at temperatures ranging from 350 to 500° C for 12 h. It was found that the hardening depth increases with increasing treatment temperature. Case depths on the order of 35 to 75 μm, can be estimated for treatments performed at 350–500°C. It is well known that the martensite hardness is a function of its carbon content, so, the hardness decrease could be important evidence that carbon diffuses as interstitial atom into the steel matrix, being an indication of the existence of a carbon concentration gradient below surface [13].

Figure 5 (b) shows the hardness profiles of the samples carburized at 400 for 12 to 24 h. It can be seen that the hardening depth increases with increasing treatment time, and case depths on the order of 50 to 85 can be estimated for treatments performed at 24–48 h, respectively. The hardness profiles of the other studied conditions can be viewed in [13].

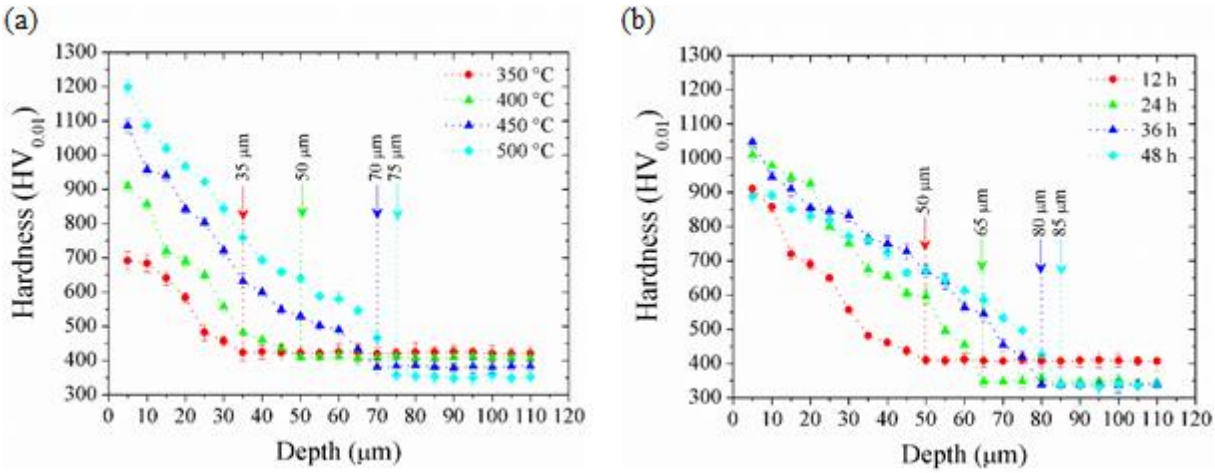

Figure 5. Hardness profile of AISI 420 steel samples plasma carburizing at 350 to 500°C for 12 h (a); and for 12 to 24 h at 400°C (b).

3.2 Influence of micro-abrasive wear test variables (first part)

3.2.1 Effect of abrasive particle size

In a free ball micro-abrasion wear tests, the steady-state wear is reached when the wear coefficient (*k*) becomes constant with sliding distance (*d*) [19]. In this regard, Figure 6 (a) shows the variation of the *k* with *d* for tribological tests conducted employing abrasive particles of 0.05, 0.3 and 1.0 μm. It is noted that the steady-state wear is reached on different sliding distances for the different conditions studied, which is increased with the decrease in abrasive particles size. It also can be seen that for smallest sliding distances, the *k* values exhibit a random behavior (transient wear regime). As described by Cozza [25], there is no fixed sliding distance for obtaining the steady-state wear, since this depends on the characteristics of the tribological system. Therefore, it is important to consider the effect of samples surface morphology (structure and composition) on the wear regime. In this context, in Figure 6 (b) is illustrated variation of worn crater depth as a function of abrasive particle size. It is possible to observe a direct relation between the outer layer thickness and the wear crater depth from which the steady-state wear is achieved, and in all cases, the system enters steady-state after at a wear depth greater than the outer layer thickness (in Figure 6 (b), the outer layer thickness is indicated by the horizontal dashed line). As previously showed in Figure 1, the carburized layer consist of an outer layer (composed by Fe_3C and α'_C phases), and of a diffusion layer (which is formed only by α'_C). Thus, it is believed that the cementite promotes a decrease in toughness of the outer layer, increasing the wear rate. Moreover, on the diffusion layer region, the wear rate decrease occurs due to the compressive residual stresses introduction in the martensite lattice, which overlap the stresses generated during the wear test.

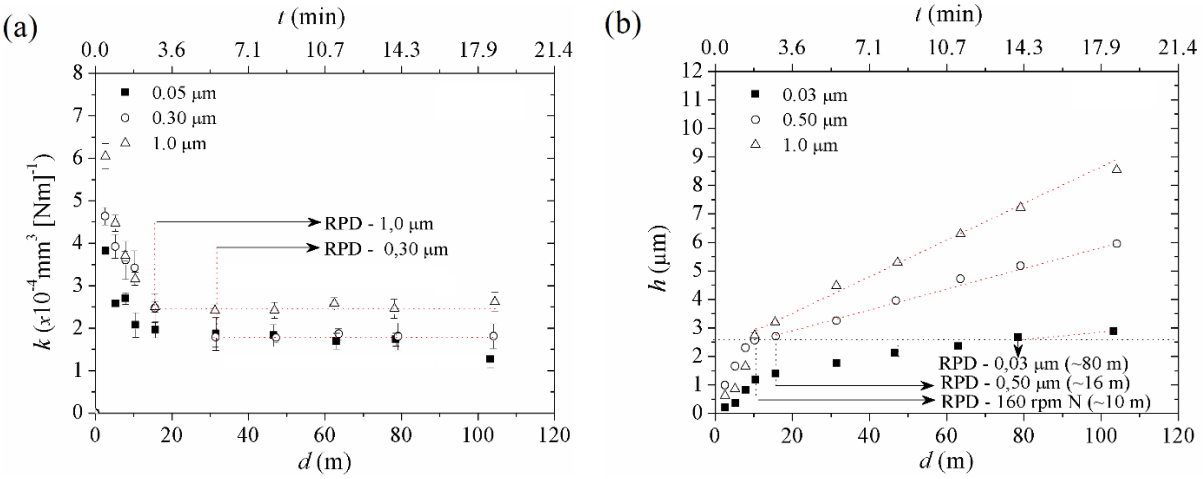

Figure 6. Evolution (a) wear coefficient; and (b) worn crater depth as a function of the sliding distance.

Figure 7 (a) shows the wear volume evolution as a function of the sliding distance for the different abrasive particle size. It can be seen that after the steady-state wear, worn volume increases linearly with the sliding distance, being increased with increasing the abrasive size. This difference is due, as above explained, to the difference in composition and morphology of the outer layer and diffusion layer.

Figure 7 (b) shows the variation of the wear rate (*Q*) and wear coefficient (*k*) as a function of abrasive size. The *k* values were determined from Figure 6 (a), considering the reach of steady-state wear. Since the *Q* values were determined by

the data linearization of the function $V = f(L, N)$, present in Figure 7 (a). It can be seen that both the wear rate and wear coefficient grow with particles size increasing. This result probably relates to the largest abrasive-sample interaction area, which is increasing with the size of the abrasive particles. This result is consistent with that presented by Sasada [26], which showed that the critical size (size of the abrasive particles from which the wear coefficient becomes constant) takes place from 50 μm.

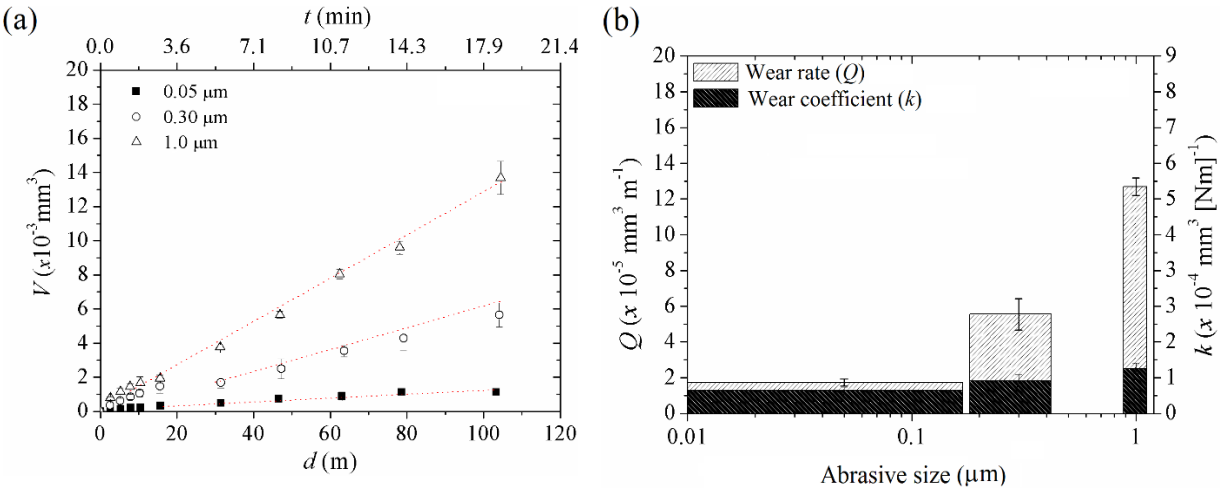

Figure 7. (a) Evolution of the wear volume as a function of the sliding distance; and (b) Wear rate and wear coefficient as a function of applied load.

The wear craters morphologies generated in the carburized sample after a sliding distance of (1) 10 and (2) 104 m, using abrasives particles sizes of (a) 0.05, (b) 0.3, and (c) 1.0 μm are shown in Figure 8. It can be note the occurrence of grooving and micro-rolling abrasion wear mechanisms. It may be verify out that an increasing on abrasive particles size promotes a reduction on the action of micro-rolling abrasion wear mechanism, and an increasing on grooving abrasion wear mode action. In this case, it is assumed that the less dispersion of particles size, associated with the highest number of small-sized abrasive particles, are responsible for the high influence of the micro-rolling wear mechanism mode, with decreasing size of the abrasive species. With the increase in the abrasive particle size, the greater dispersion of size, combined with the major number of larger particles, are responsible for the most prominent effect of grooving wear mode, with increasing size of the abrasive species.

By comparing the micrographs, it can be see that the performance of the micro-rolling wear mechanisms increases with increasing sliding distance. This result can be explained considering that at the beginning of the test, contact pressure is relatively high, and in these circumstances, it is more difficult to the abrasive particles roll over. With the increase in the sliding distance the worn area is increased and so the contact pressure decreases, favoring the rotation movement of the abrasive particles. Thus, develops favorable conditions for a higher amount of abrasive particles become interposed in the contact region between samples surface and counterbody, collaborating in the material removing process. Furthermore, the increase in the abrasive portion in the ball-sample contact zone, favors the reduction of the normal force value acting on each abrasive, which favors the acting of rolling wear mode.

It can also be noted from Figure 7 that with the sliding distance increasing, the number and depth of grooves also suffer increased. In this case it is assumed that the increase in test time provides that larger quantity of abrasive particles transpassive through the ball-sample interface, promoting additional quantity of scratch observed. This fact is powered mainly by the increase in abrasive particles retention in the upper region of the sphere-samples contact interface, which was checked during the tests. Moreover, another possible cause may be related to an increase with the sliding distances of the number and depth of the grooves, that occurs due to the reduction in hardness with increasing depth of crater wear (see Figure 5). Thus, the greater the depth of the crater, the greater susceptibility of the material to be strained, due to the reduction of mechanical properties which occur along its cross section, as shown in Figure 5.

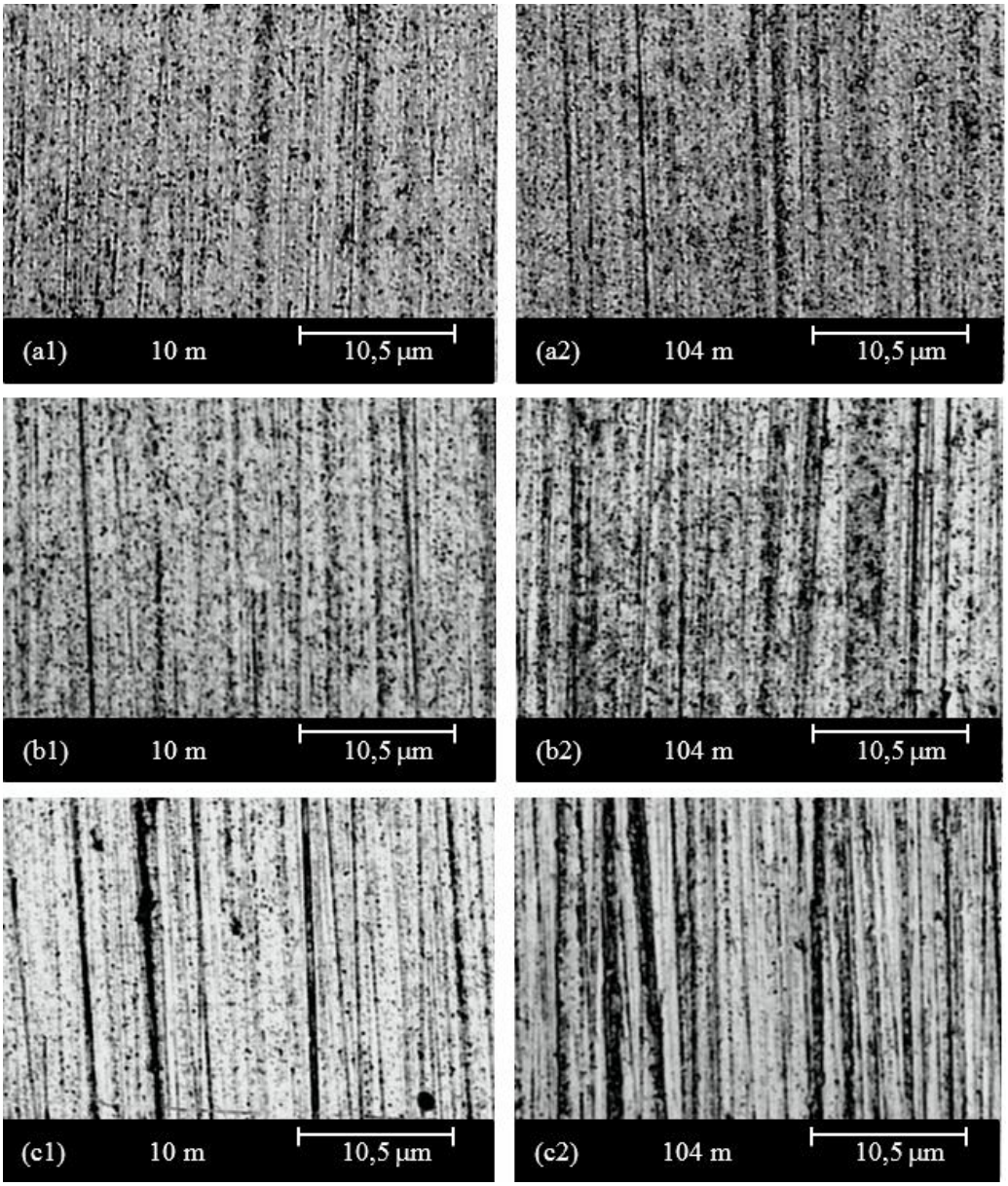

Figure 8. Wear scars morphology of worn craters produced at sliding distances of (1) 10 m and (b) 104 m, for abrasive particle size of (a) 0.05, (b) 0.3 an (c) 1.0 µm.

3.2.2 Effect of counter body rotation speed

Figure 9 (a) shows the variation of the *k* with *d* for tribological tests conducted employing ball rotation speeds of 80, 120 and 160 rpm. It is noted that the steady-state wear is reached on different sliding distances, for the different conditions studied, which is increased with increased ball rotation speed. It also can be seen that for smallest sliding distances, the *k* values exhibit a random behavior (transient wear regime), as previously shown in Figure 6 (a).

In Figure 9 (b) is illustrated variation of worn crater depth as a function of ball rotation speed. As already pointed out earlier (Figure 6 (b)), it is possible to observe a direct relation between the outer layer thickness and the wear crater depth from which the steady-state wear is achieved, and in all cases, the system enters steady-state after at a wear depth greater than the outer layer thickness. As explained earlier, this behavior is due to the morphological dissimilarity between these regions

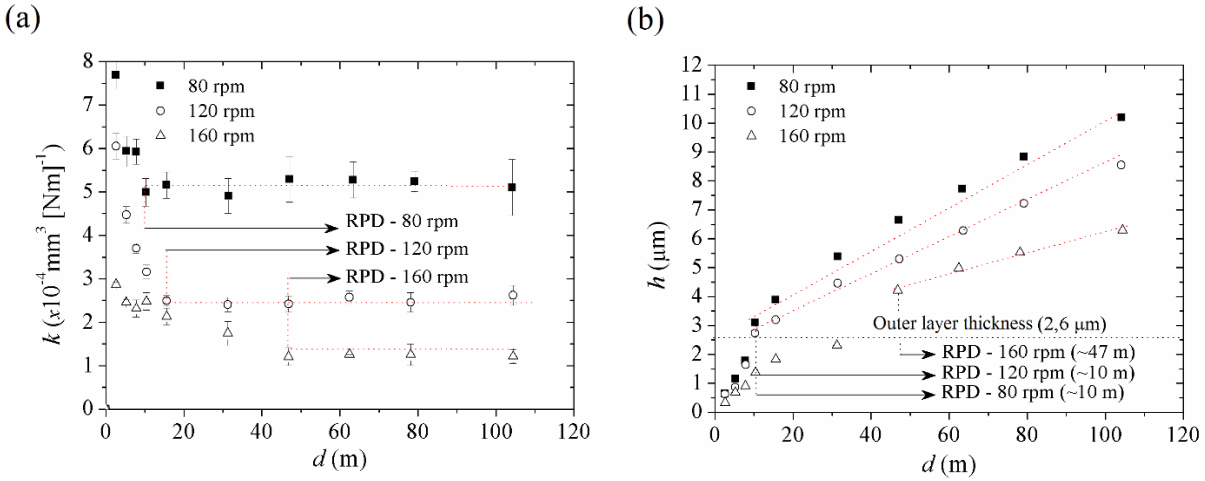

Figure 9. Evolution (a) wear coefficient; and (b) worn crater depth as a function of the sliding distance.

Figure 10 (a) shows the wear volume evolution as a function of the sliding distance for the different ball rotation speed. It can be seen that after the steady-state wear, worn volume increases linearly with the sliding distance, being increased with increasing applied normal load. This difference is due, as above explained, to the difference in composition and morphology of the outer layer and diffusion layer. Figure 10 (b) shows the variation of the wear rate (*Q*) and wear coefficient (*k*) as a function of ball rotation speed (*n*). The *k* values were determined from Figure 9 (a), considering the reach of steady-state wear. Since the *Q* values were determined by the data linearization of the function $V = f(L, N)$, present in Figure 10 (a). Note that both the wear rate and coefficient decrease with the increase of the counter-body rotational speed, indicating the dependence of these two factors on the studied variable. Bello and Wood [16] showed a similar results in polyamine coating, and the authors credited this behavior to hydrodynamic effects that occur between samples and counter body during the sliding. This explanation seems plausible, since, with the formation of a hydrodynamic film between the specimen and the ball, it decreases the abrasive interaction with the sample, thereby reducing the volume of material removed by micro-abrasion.

With respect to the worn craters morphology, the occurrence of grooving abrasion and micro-rolling abrasion wear mechanisms was verified, with similar appearance to those shown in Figure 8.

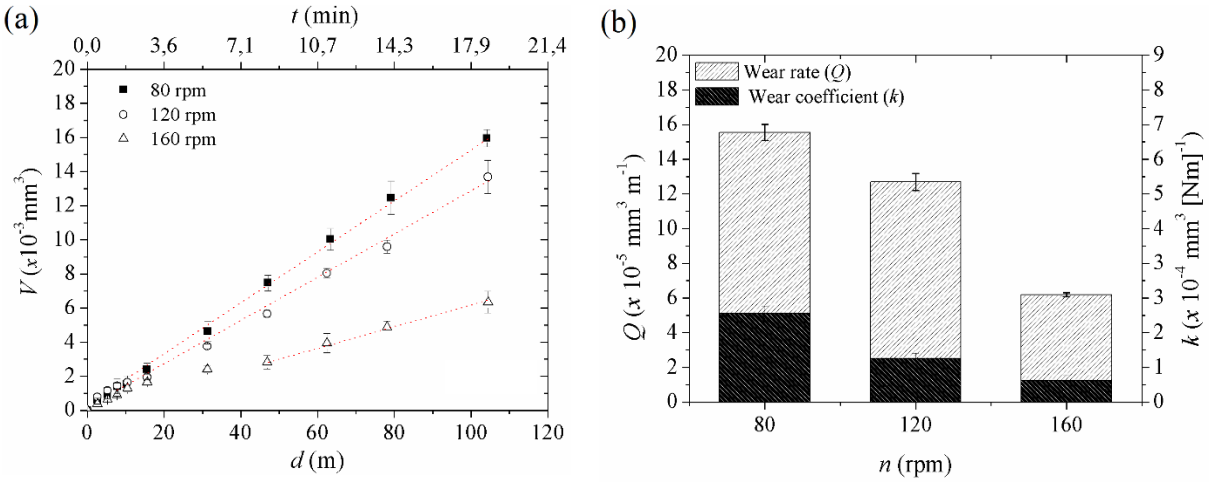

Figure 10. (a) Evolution of the wear volume as a function of the sliding distance; and (b) Wear rate and wear coefficient as a function of applied load.

3.2.3 Effect of normal load

The variation of the wear coefficient and worn crater depth with sliding distance for tribological tests conducted employing normal loads of 0.1, 0.3 and 0.5 N is showed in Figure 11 (a,b), respectively. Keeping the same pattern already illustrated in Figure 6 (a) and Figure 9 (a), the steady-state wear is reached after at a wear depth greater than the outer layer thickness, confirming the already shown effect of microstructure and surface chemistry on the tribological behavior.

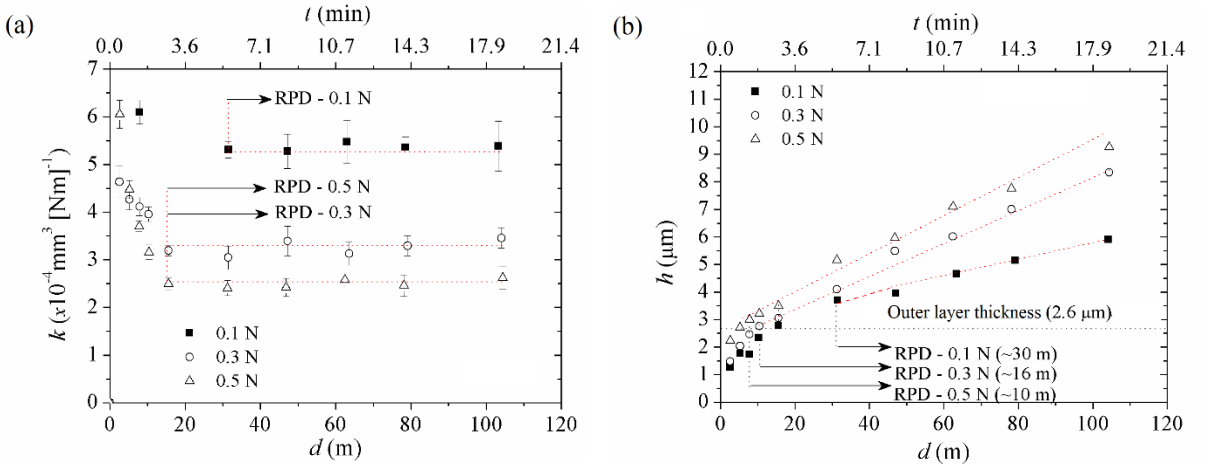

Figure 11. Evolution (a) wear coefficient; and (b) worn crater depth as a function of the sliding distance.

The wear volume evolution as a function of the sliding distance for the different applied normal load is shown in Figure 12 (a). It can be seen that after the steady-state wear, worn volume increases linearly with the sliding distance, being increased with increasing applied normal load. Figure 7 (b) shows the variation of the wear rate and wear coefficient as a function of applied normal load. It can be seen that both varies linearly with the normal load: the Q values increase, while k values decrease with the load increase. Both results are in agreement with data previously published by Bose and Woo [18]. Considering that the Archard law [26] states that the wear volume is proportional to the applied load ($V = f(N)$), and considering that Q is proportional to the ratio between the wear volume and sliding distance ($Q = f(V/S)$),

and whereas the value of k is a function of ratio between the wear volume and the normal load and sliding distance product ($k = f(V/N.S)$), or simply $k = f(Q/N)$, is consistent that the progressive increase of *S* and *N* promote a linear change in the values of *Q* and *k*.

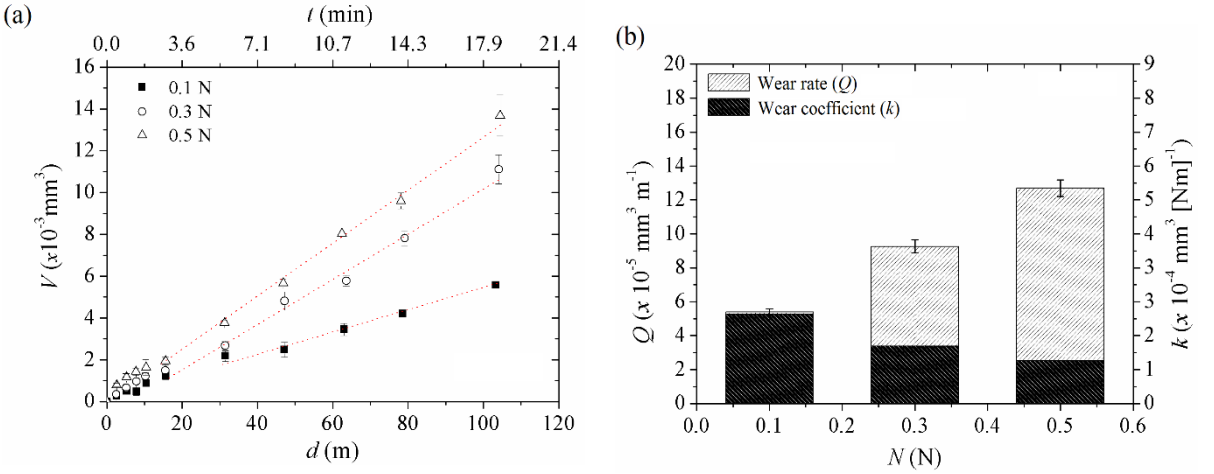

Figure 12. (a) Evolution of the wear volume as a function of the sliding distance; and (b) Wear rate and wear coefficient as a function of applied load.

As regards to the worn craters morphology, the grooving abrasion and micro-rolling abrasion wear mechanisms was observed, with similar appearance to those shown in Figure 8.

3.3 Influence of plasma process variables (second part)

In Figure 13 (a,b) is shown the wear rate (Q) and wear coefficient (k) in the steady-state wear, as a function of the carburizing temperature for samples treated for 8 and 12 h, respectively. It is possible to observe a similar behavior for the wear rate and wear coefficient in the two cycles of times studied: both suffer reduced within in the treatment temperature range of 350 to 450 °C, with subsequent increasing to the treatment condition of 500°C. A reduction in the *Q* and *k* values within the first range, is related to the increase of the carbon content retained in solid solution with the addition of the treatment temperature, with a consequent increase in the compressive residual stress on the carburized layer region [27]. On the other hand, the increase in the *Q* and *k* values for sample treated at 500°C condition occurs due to precipitation of chromium carbide, which reduces the retained C content in solid solution in the TCC cell interstices, decreasing compressive residual stress, and the wear resistance [16].

In Figure 14 (a,b) the wear rate (Q) and wear coefficient (k) in the steady-state wear, are shown as a function of the carburizing time for samples treated at 400 °C and 450 °C, respectively. A similar behavior for the wear rate and wear coefficient can be observed in the two cycles of temperature studied: both suffer reduced within in the treatment temperature range of 12 to 36 h (for treatment performed at 400 °C) and 4 to 12 h (for treatment performed at 450 °C), with subsequent increasing to the treatment condition of 48 and 16 h, respectively. This result is also being linked to the increased carbon content in solid solution with treatment time, and to martensite phase decomposition held for very prolonged treatment times.

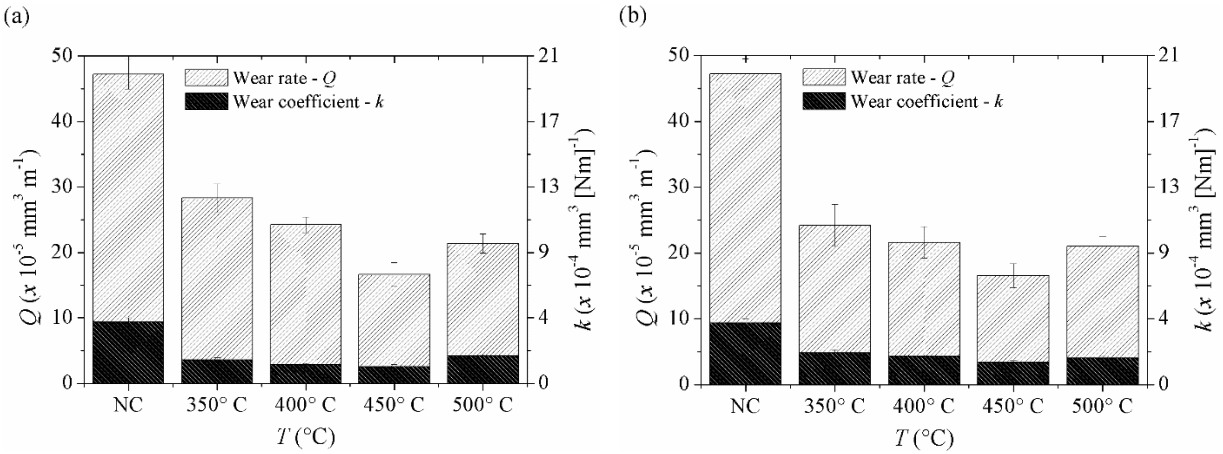

Figure 13. Wear rate and wear coefficient as a function of carburizing temperature for treatments performed at (a) 8 and (b) 12 h

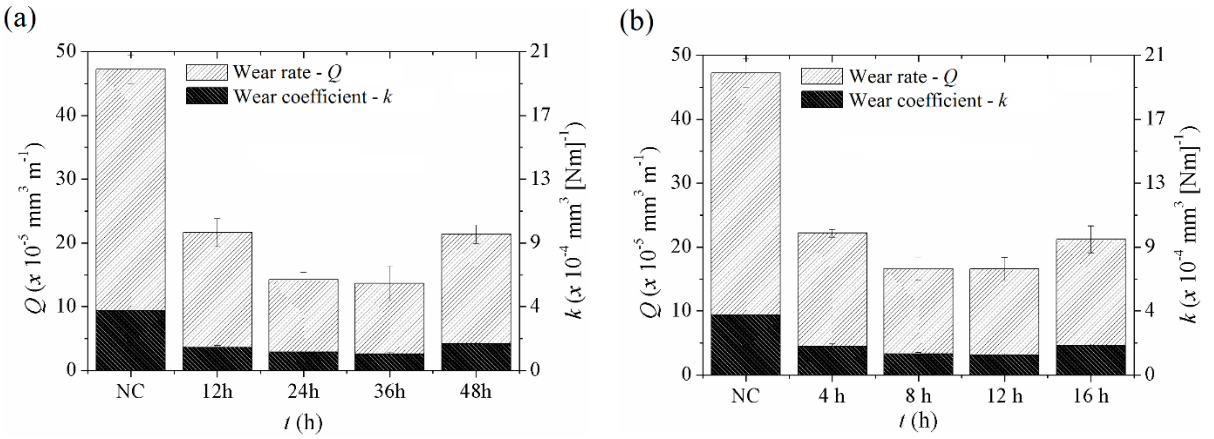

Figure 14. Wear rate and wear coefficient as a function of carburizing temperature for treatments performed at (a) 400 °C and (b) 450 °C

Finally, the occurrence of grooving abrasion and micro-rolling abrasion wear mechanisms was verified, with similar appearance to those shown in Figure 8.

4 CONCLUSION

Based on the presented and discussed results it can be concluded that:

- The wear mechanisms predominant were the grooving and micro-rolling modes;
- The carburized layer morphology influences on the micro-abrasion wear behavior of the treated material;
- The steady-state wear is reached only after the worn crater depth exceed the outer layer thickness;
- The wear rate and wear coefficient increased with increasing the particle abrasive size and normal load; and decrease with rise of counter body rotation speed;
- The acting of micro-rolling abrasion and grooving abrasion wear modes increases with increasing the sliding distance; and

- For high temperature and prolonged treatment times, wear rate and wear coefficient increase as a function of intense chromium carbide precipitation.

Acknowledgments

This work was supported by CNPq, CAPES-COFECUB and *Programa Interdisciplinar de Petróleo e Gás Natural da UFPR* (PRH24). The authors also wish to express their thanks to the Laboratory of X-ray Optics and Instrumentation — LORXI, from the UFPR by the use of the X-ray diffraction equipment.

REFERENCES

1. Basso RLO, Candal RJ, Figueroa CA, Wisnivesky D, Alvarez F. Influence of microstructure on the corrosion behavior of nitrocarburized AISI H13 tool steel obtained by pulsed DC plasma. Surface and Coatings Technology. 2009; 203: 1293 – 1297.
2. Li CX, Bell T. Corrosion properties of plasma nitride AISI 410 martensitic stainless steel in 3.5% NaCl and 1% HCl aqueous solutions. Corrosion Science. 2006; 48: 2036–2049.
3. Lei MK, Zhang ZL. Plasma source ion nitriding - a new low-temperature, low-pressure nitriding approach. Journal of Vacuum Science and Technology A. 1995; 13: 2986–2990
4. Rolinski E. Effect of Plasma Nitriding Temperature on Surface Properties of Austenitic Stainless Steel, Surface Engineering. 1987; 3(1): 35-40.
5. Zhang ZL, Bell T. Structure and corrosion resistance of plasma nitrided stainless steel. Surface Engineering. 1985; 1 (2): 131-136.
6. Corengia P, Walther F, Ybarra G, Sommadossi S, Corbari R, Broitman, E. Friction and rolling–sliding wear of DC-pulsed plasma nitride AISI 410 martensitic stainless steel. Wear. 2006; 260: 479–485.
7. Xi YT, Liu DX, Han D. Improvement of corrosion and wear resistances of AISI 420 martensitic stainless steel using plasma nitriding at low temperature. Surface & Coatings Technology. 2008; 202: 2577–2583.
8. Corengia P, Ybarra G, Moina C, Cabo A, Broitman E. Microstructure and corrosion behaviour of DC-pulsed plasma nitride AISI 410 martensitic stainless steel**.** Surface & Coatings Technology. 2004; 187: 63–69.
9. Li CX, Bell T. Corrosion properties of plasma nitride AISI 410 martensitic stainless steel in 3.5% NaCl and 1% HCl aqueous solutions. Corrosion Science. 2006; 48(8): 2036–2049.
10. Xi YT, Liu DX, Han D. Improvement of mechanical properties of Martensitic stainless steel by plasma nitriding at low temperature. Acta Metall. Sin.(Engl. Lett.). 2008; 21(1): 21–29.
11. Scheuer CJ, Cardoso RP, Pereira R, Mafra M, Brunatto SF. Low temperature plasma carburizing of martensitic stainless steel. Materials Science and Engineering A, 2012; 539: 369–372.
12. Scheuer CJ, Cardoso RP, Zanetti FI, Amaral T, Brunatto SF. Low-temperature plasma carburizing of AISI 420 martensitic stainless steel: Influence of gas mixture and gas flow rate. Surface and Coatings Technology, 2012; 206: 5085–5090.
13. Scheuer CJ, Cardoso RP, Pereira R, Mafra M, Brunatto SF. AISI 420 martensitic stainless steel low-temperature plasma assisted carburizing kinetics. Surface and Coatings Technology, 2013; 24: 30–37.
14. Bello JO, Wood RJK. Micro-abrasion of filled and unfilled polyamide 11 coatings, Wear, 2005; 259:1157-1167.
15. Bello JO, Wood RJK. Grooving micro-abrasion of polyamide 11 coated carbon steel tubulars for downhole application. Wear, 200. 255: 1157-1167.
16. Bose K, Wood, RJK. Optimun test conditions for attaining uniform rolling abrasion in ball cratering test on hard coatings. Wear, 2005; 258: 322-332.

17. Adachi K, Hutchings IM. Sensivity of wear rates in the micro-scale abrasion test to test conditions and materials hardness. Wear, 2005; 258: 318-321.
18. Bose K, Wood RJK, Influence of load and speed on rolling micro-abrasion of CVD diamond and other hard coatings. Diamond and Related Materials, 2003; 12:753-756.
19. Trezona RI, Allsopp DN, Hutchings IM. Transitions between two-body and threebody abrasive wear: influence of test conditions in the microscale abrasive wear test. Wear, 1999; 225: 205-214.
20. Shipway PH, Hogg JJ. Dependence of microscale abrasion mechanisms of WC-Cohardmetals on abrasive type. Wear, 2005; 259: 44-51.
21. Thakare MR, Wharton JA, Wood RJK, Menger C. Exposure effects of strong alkaline conditions on the microscale abrasion-corrosion of D-gun sprayed WC-10Co-4Cr coating. Tribology International, 2008; 41: 629-639.
22. Gee MG, Gant AJ, Hutchings IM, Bethke R, Schiffman K, Van Acker K, Poulat S, Gachon Y, Stebut J, Progress towards standardisation of ball cratering. Wear, 2003; 255: 1-13.
23. Adachi K, Hutchings IM. Wear-mode mapping for the micro-scale abrasion test. Wear, 2003; 255: 23-29.
24. Schiffmann KI, Bethke R, Kristen N. Analysis of perforating and non-perforating micro-scale abrasion tests on coated substrates. Surface and Coatings Technology. 2005; 200: 2348-2357
25. Cozza RC. Estudo do comportamento do coeficiente de desgaste e dos modos de desgaste abrasivo em ensaios de desgaste micro-abrasivo. 217 f. Dissertação (Mestrado em Engenharia Mecânica), Universidade de São Paulo, São Paulo, 2006.
26. Sasada T, Oike M, Emori N. The effect of abrasive grain size on the transition between abrasive and adhesive wear. Wear, 1994; 97: 291-302.
27. Qasmi M.; Delobelle P.; Richard F.; Bosseboeuf A. Effect of the residual stress on the determination through nanoindentation technique of the Young's modulus of W thin film deposit on SiO2/Si substrate. Surface and Coatings Technology, v. 200(14-15), pp. 4185–4194, 2006.